Time-dependent greenhouse warming computations with a coupled ocean-atmosphere model

Ulrich Cubasch[1], Klaus Hasselmann[2], Heinke Höck[2], Ernst Maier-Reimer[2], Uwe Mikolajewicz[2], Benjamin D Santer[2], and Robert Sausen[3]

[1] DKRZ, Bundesstrasse 55, W-2000 Hamburg 13, FRG
[2] Max-Planck-Institut für Meteorologie, Bundesstrasse 55, W-2000 Hamburg 13, FRG
[3] DLR, Institut für Physik der Atmosphäre, W-8031 Oberpfaffenhofen, FRG

Abstract. Climate changes during the next 100 years caused by anthropogenic emissions of greenhouse gases have been simulated for the Intergovernmental Panel on Climate Change Scenarios A ("business as usual") and D ("accelerated policies") using a coupled ocean-atmosphere general circulation model. In the global average, the near-surface temperature rises by 2.6 K in Scenario A and by 0.6 K in Scenario D. The global patterns of climate change for both IPCC scenarios and for a third step-function $2 \times CO_2$ experiment were found to be very similar. The warming delay over the oceans is larger than found in simulations with atmospheric general circulation models coupled to mixed-layer models, leading to a more pronounced land-sea contrast and a weaker warming (and in some regions even an initial cooling) in the Southern Ocean. During the first forty years, the global warming and sea level rise due to the thermal expansion of the ocean are significantly slower than estimated previously from box-diffusion-upwelling models, but the major part of this delay can be attributed to the previous warming history prior to the start of present coupled ocean-atmosphere model integration (cold start).

Introduction

Detailed numerical simulations to estimate the climate change caused by increasing greenhouse gases have largely been performed in the past with atmospheric general circulation models (AGCMs) coupled to a simple mixed-layer ocean with a depth of typically 50 m (Wilson and Mitchell 1987; Schlesinger and Mitchell 1987; Wetherald and Manabe 1988; Washington and Meehl 1989b) or to a model which parameterizes heat transport below the mixed-layer as a diffusive process (Hansen et al. 1988). A shortcoming of models of this kind is that they are unable to simulate the impact of a climate change on the ocean circulation, in particular on

the oceanic heat transport and on the storage of heat in the deep ocean. These processes have a strong influence both on the equilibrium climate and on the transient climate response to external forcing. It is, therefore, generally recognized that reliable estimates of the response to greenhouse warming can be achieved only with simulations using fully coupled atmosphere-ocean general circulation models (Houghton et al. 1990).

Three such experiments have recently been carried out (Washington and Meehl 1989a; Stouffer et al. 1989; Manabe et al. 1991; Houghton et al. 1992). The order of magnitude of the global warming predicted by atmosphere-mixed-layer models is confirmed in these experiments. The transient response patterns are not dissimilar to the patterns produced by equilibrium integrations, but the land-sea contrast is more pronounced and the warming over the northern North Atlantic and particularly the Southern Ocean is strongly reduced.

The present paper considers three further time-dependent greenhouse warming simulations together with a reference control experiment using one of the Hamburg coupled global atmosphere-ocean general circulation models. The main motivation for this study is the recent report (Houghton et al. 1990) of Working Group 1 of the Intergovernmental Panel on Climate Change (IPCC), which discusses four greenhouse gas scenarios ranging from the "business as usual" Scenario A, in which emissions are allowed to increase unrestricted, through a set of successively more stringent abatement policies to the severest emission reduction Scenario D (Figure 1). The IPCC scenarios are intended to provide the scientific basis for future international negotiations on the development of viable global climate policies which may have far-reaching economic implications. Since coupled ocean-atmosphere model simulations using these scenarios could not be carried out within the time frame of the IPCC study, however, the published IPCC scenarios had to be based on highly simplified box-diffusion-upwelling models (Wigley and Raper 1987). In the present study we present some results using a more realistic coupled ocean-atmosphere model for the two limiting Scenarios A and D.

Correspondence to: K Hasselmann

In addition, we have computed the transient response of the coupled system to a sudden increase of the atmospheric CO_2 concentration. This provides a comparison with equilibrium response computations for doubled CO_2 levels performed previously with atmosphere-mixed-layer ocean models. Originally, another motivation of the experiment was to derive the impulse response characteristics of the coupled system, which are useful for general theoretical transient response studies. However, it was subsequently found that the response in this experiment was too strongly nonlinear for this purpose, so that the impulse response functions were inferred instead from the Scenario A experiment (Hasselmann et al. 1992).

The coupled model

The atmospheric and oceanic components of the coupled model have been tested and applied in a variety of climate experiments (Hasselmann 1991), such as the ocean response to stochastic forcing (Mikolajewicz and Maier-Reimer 1990), paleoclimatic studies (Maier-Reimer and Mikolajewicz 1989; Lautenschlager and Herterich 1990), and the atmospheric response to changes in radiative forcing (Cess et al. 1989). In the coupled mode, the models were applied in a recent investigation (Bakan et al. 1991) of the climatic impact of burning oil wells in Kuwait.

The atmosphere component (ECHAM-1) consists of a low resolution version of the spectral numerical weather forecasting model of the European Centre for Medium Range Weather Forecasts which has been modified extensively in Hamburg for climate applications (ECHAM). The prognostic variables are vorticity and divergence, temperature, surface pressure, water vapour and cloud water (droplets and crystals). The introduction of cloud water as an additional prognostic variable enables a more realistic simulation of clouds, precipitation and radiation (Roeckner et al. 1989). The diurnal cycle is included. Sub-grid scale physical processes such as radiation, cloud formation, precipitation, convection and turbulent mixing are parameterized. The runoff into the ocean is calculated using a simple surface hydrology model (Sausen personal communication).

In the current study, the horizontal resolution is limited by a triangular spectral cut-off at total wave number 21. The spectral representation is transformed to a 5.6° Gaussian grid to calculate the non-linear advection terms and physical processes. Vertically, the model is discretized on 19 levels in a hybrid σ-p-system. The semi-implicit integration scheme uses a time step of 40 minutes.

The ocean component (LSG) is based on a numerical formulation of the primitive equations (Maier-Reimer and Hasselmann 1987; Mikolajewicz and Maier-Reimer 1990; Maier-Reimer et al. 1992) appropriate for large-scale geostrophic motion. The nonlinear advection of momentum is neglected and fast gravity waves are strongly damped by an implicit time integration scheme using a time step of 30 days. The salinity and tempera-

ture transport through currents is computed with an upstream advection scheme. A small explicit horizontal diffusion of 200 m²/s is introduced to counteract the inherent tendency for mode-splitting in the E-grid used in the horizontal discretization scheme. Vertical convective mixing is applied whenever the stratification becomes unstable (mainly in high latitudes, where strong surface cooling occurs). Sea ice is computed from the ice heat balance and the advection by oceanic currents, using a simplified viscous rheology. A realistic bottom topography is included.

In the present simulations, the discretization of the ocean model is based on 11 variably spaced vertical levels (centered at depths of 25, 75, 150, 250, 450, 700, 1000, 2000, 3000, 4000 and 5000 m) and two overlapping $5.6° \times 5.6°$ horizontal grids (corresponding to an effective net grid-size of 4°), which are interpolated onto the Gaussian grid used in ECHAM. In the coupled model simulations, the basic time step of 30 days is reduced to 1 day for the computation of sea ice and the temperature and salinity in the two uppermost ocean levels in order to resolve the more rapid response of the upper ocean to the short-term variability of the atmosphere.

Before coupling, the ocean model was integrated for 5000 years in a spin-up run using salinity boundary conditions which restored the surface salinity to the Levitus (1982) data set. The diagnosed fresh water fluxes from this run were then used as external forcing for a subsequent integration of 2000 years. The final state of this integration was then used as the initial state for the model coupling.

The atmosphere and ocean components are coupled by the air-sea fluxes of momentum, sensible and latent heat, short and long wave radiation and fresh water (evaporation minus precipitation, plus runoff along the coastal boundaries). The fluxes are calculated in ECHAM, using as surface boundary conditions the sea surface temperature and sea ice thickness (from which the sea ice skin temperature is computed).

To avoid a climate drift of the coupled system, a flux correction is applied (Sausen et al. 1988). This is equivalent to coupling the atmosphere and ocean in anomaly response experiments by the anomalies of the fluxes computed relative to the equilibrium states of the un-
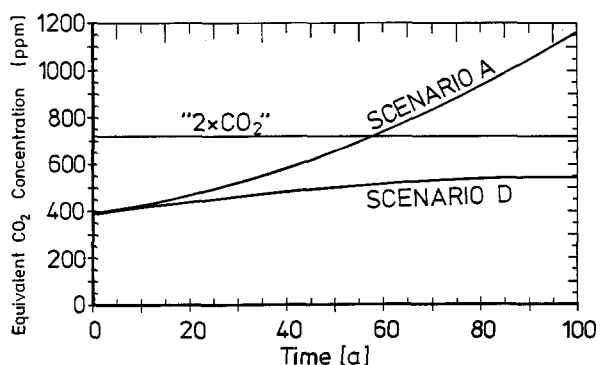

Fig. 1. Time evolution of the equivalent CO_2 concentration in the IPCC Scenarios A and D and the $2 \times CO_2$ experiment

a)

b)
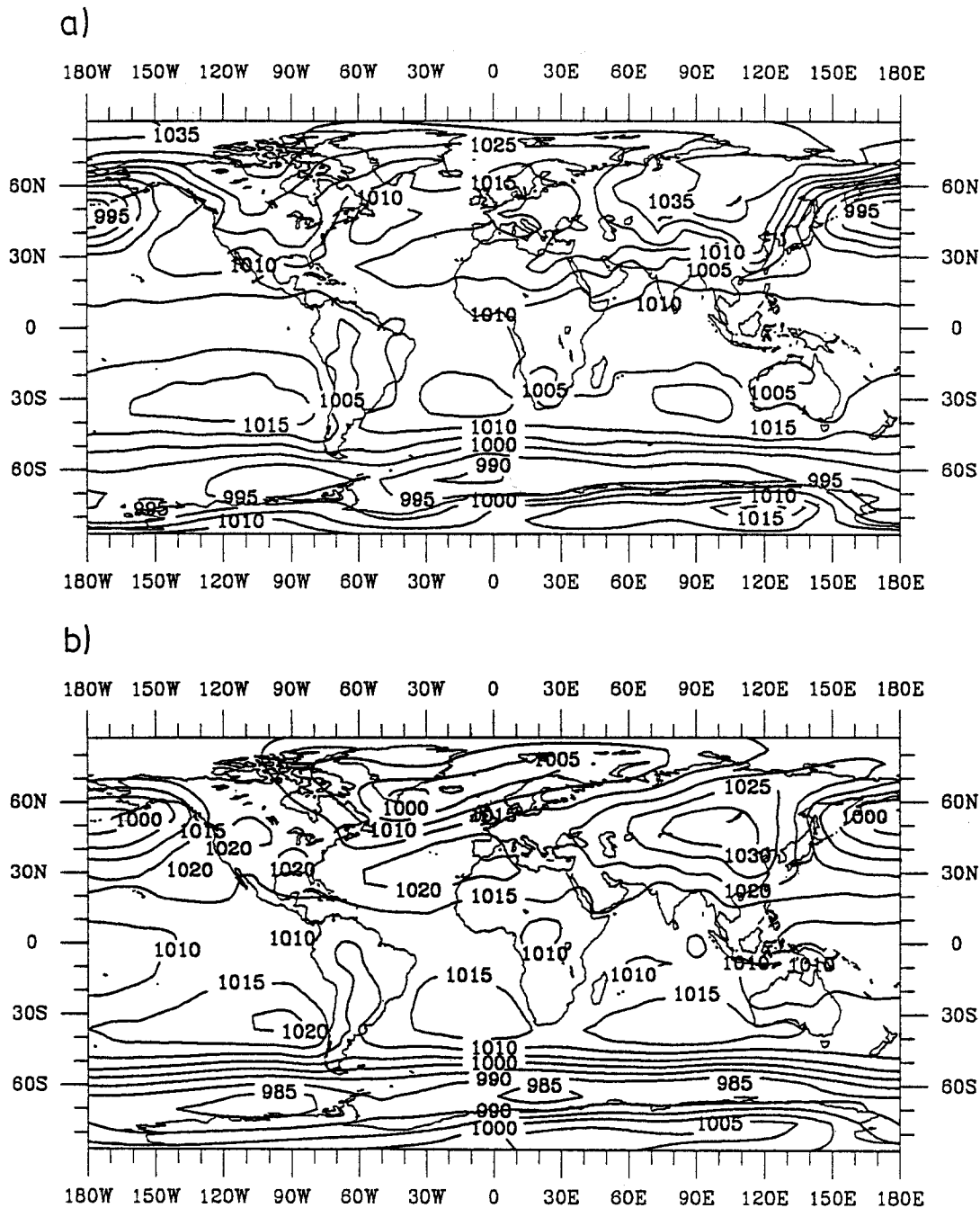
Fig. 2a, b. Geographical distribution of sea level pressure (hPa) for the winter season (DJF) in the final decade (years 91–100) **a** of the control simulation and **b** in the observations. The observed data are based on ECMWF analyses from 1979–88

coupled sub-systems. The flux correction has no impact on the computed response for small perturbations about the mean state of the model climate, provided the individual sub-systems reproduce the mean climate reasonably well.

Both models are integrated synchronously, but with their different time steps. Thus the fluxes computed at each 40 minute time step of the atmospheric model are summed over one full time step of the ocean model (1 day for the upper layers, including sea ice) and are then transferred to the uppermost layer of the ocean model.

Numerical simulations

All simulations were carried out over a 100-year period. In addition to the three greenhouse warming experiments (IPCC Scenarios A, D and $2 \times CO_2$), a control run with constant 1985 atmospheric CO_2 concentration was carried out as a reference (Fig. 1).

The control run

The general structure of the mean atmospheric circulation is simulated reasonably well in the control run, al-

a)

b)
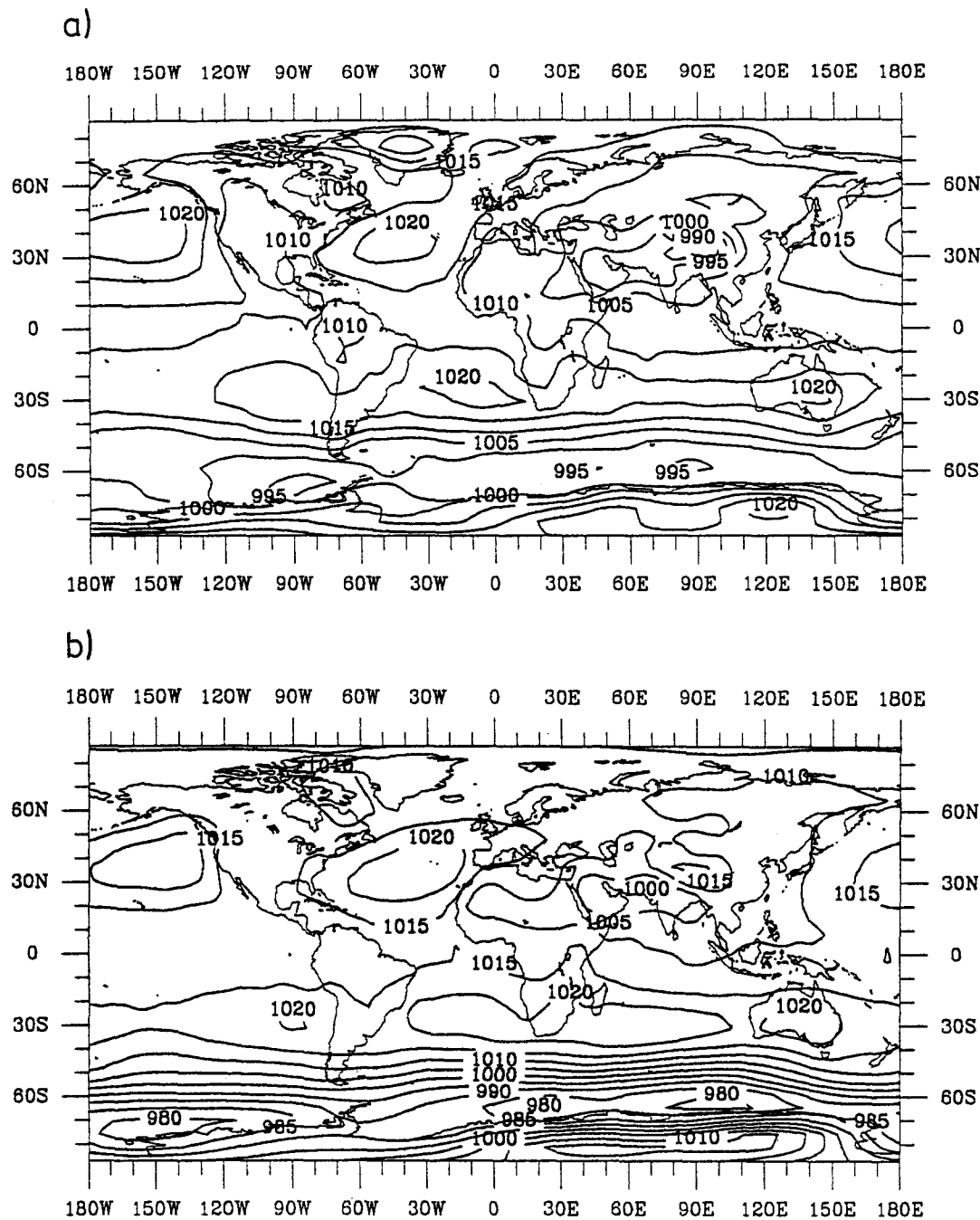
Fig. 3a, b. Geographical distribution of sea level pressure (hPa) for the summer season (JJA) in the final decade (years 91–100) **a** of the control simulation and **b** in the observations. The observed data are based on ECMWF analyses from 1979–88

though the simulation exhibits shortcomings typical of low resolution atmospheric models which are unable to adequately resolve mid-latitude baroclinic disturbances (underestimated cyclonic activity). The version of ECHAM-1 used for the coupled model simulations has a tendency to underestimate the strength of the Icelandic Low in winter, resulting in unrealistically weak westerly winds over the North Atlantic (Fig. 2). In contrast, the Aleutian Low is too deep. These problems are caused by a combination of the low resolution and the gravity wave drag parameterization. In northern summer the Northern Hemisphere subtropical highs are simulated realistically (Fig. 3). In the Southern Hemisphere the

model's equator-to-pole pressure gradient is too weak in both seasons, a feature typical of low resolution models (Xu et al. 1990).

The zonally-averaged zonal wind component is simulated realistically (Figs. 4 and 5). There is good correspondence in the magnitude and location of the observed and simulated jets in both winter and summer. The errors are generally smaller than in other atmospheric models of comparable resolution (Boer et al. 1991). At the surface the simulated winds are in close agreement with observations, except in the region polewards of 50°N, where the errors associated with the too weak Icelandic Low are seen also in the zonal averages.
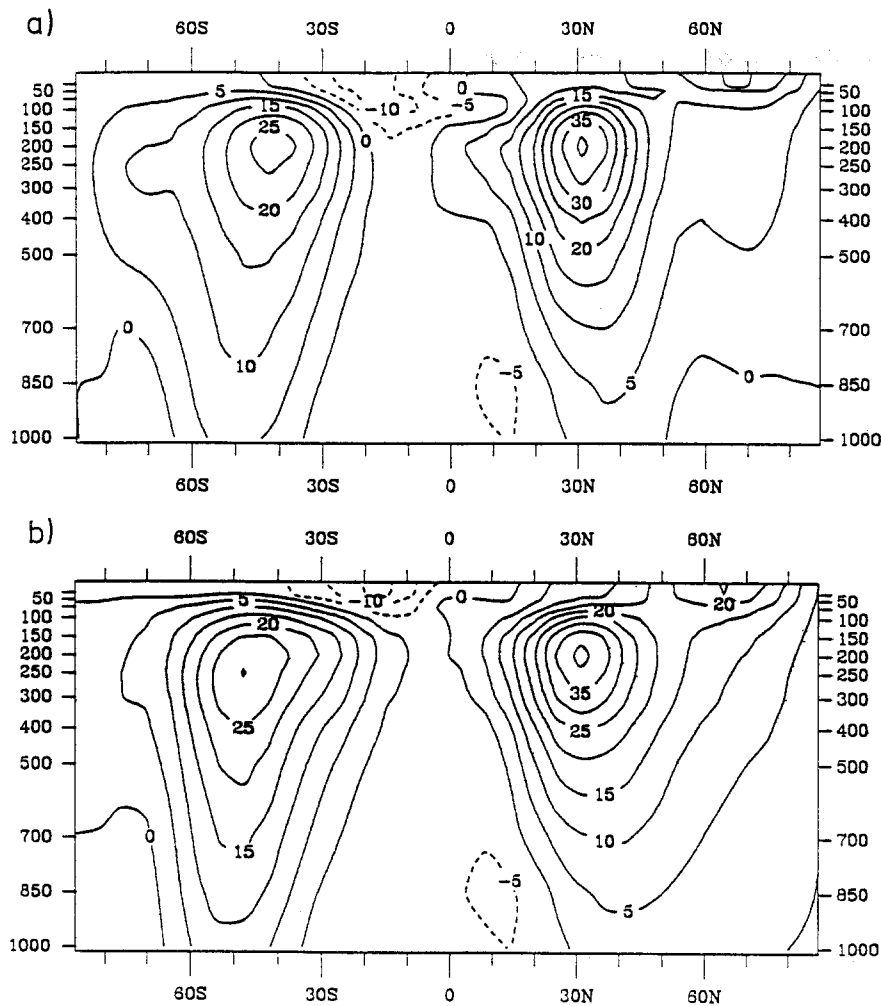
Fig. 4a, b. Zonally-averaged profile of the zonal wind component (m/s) for the winter season (DJF) in the final decade (years 91-100) a of the control simulation and b in the observations. The observed data are based on ECMWF analyses from 1979-88

In general, as expected if the flux correction is effective, the climatology of the atmospheric component of the coupled model is very similar to the climatology of the uncoupled atmospheric model, which has been documented by Boer et al. (1991) and Tibaldi and Tosi (1991).

The flux correction similarly ensures that the climatology of the oceanic component of the coupled model is essentially identical to that of the uncoupled model documented by Maier-Reimer et al. (1992). We summarize here only a few salient features of the model's ocean circulation which refer mainly to the large scale oceanic 'conveyor belt' circulation (Gordon 1986; Broecker 1987) and are thus particularly relevant for the present climate investigations.

Figure 6 shows the mean sea level, whose gradients govern the near surface and barotropic geostrophic flow, with respect to an equipotential surface. Results are given for the final decade of the control run. The structure reflects the verically integrated density distribution, which is governed primarily by temperature distribution in the upper kilometer. The lower salinity in the Pacific with respect to the Atlantic is dynamically balanced by a relative sea level enhancement of 80 cm in the Pacific. Generally, the regional structure is in good agreement with the distribution of geopotential thickness shown by Levitus (1982, Fig. 67).

The most critical quantity for a comparison with observations is the distribution of salinity, especially for intermediate water masses. Figures 7a and 8a show the salinity sections through the central Atlantic and Pacific, respectively, again for the final decade of the control run. Figures 7b and 8b show the corresponding sections for the Levitus data (1982). The most pronounced features in the Atlantic are the tongue of relatively fresh Antarctic intermediate water (AAIW) at a depth of 1 km and the high salinity plume of North Atlantic deep water (NADW). Whereas the NADW is well reproduced, the AAIW (which is linked to the high fresh water flux into the Southern Ocean) is too saline, a feature common to all coarse resolution AGCMs. At the surface, near the ice edge, the salinity is lower than the Levitus climatological value by 0.5 permille. This is due to a small shift which occurred in the ocean circulation after the salinity boundary condition was changed from the restoring condition, in which the surface salinity was forced to remain close to the Levitus data, to the flux condition, in which the stabilizing salinity feedback was removed. Although no change should occur theoretically for a completely time independent circulation state, in practice the small stochastic perturbations associated with the time dependent convective mixing events slightly modified the mean circulation after the stabilizing salinity constraint was switched off.

a)

b)
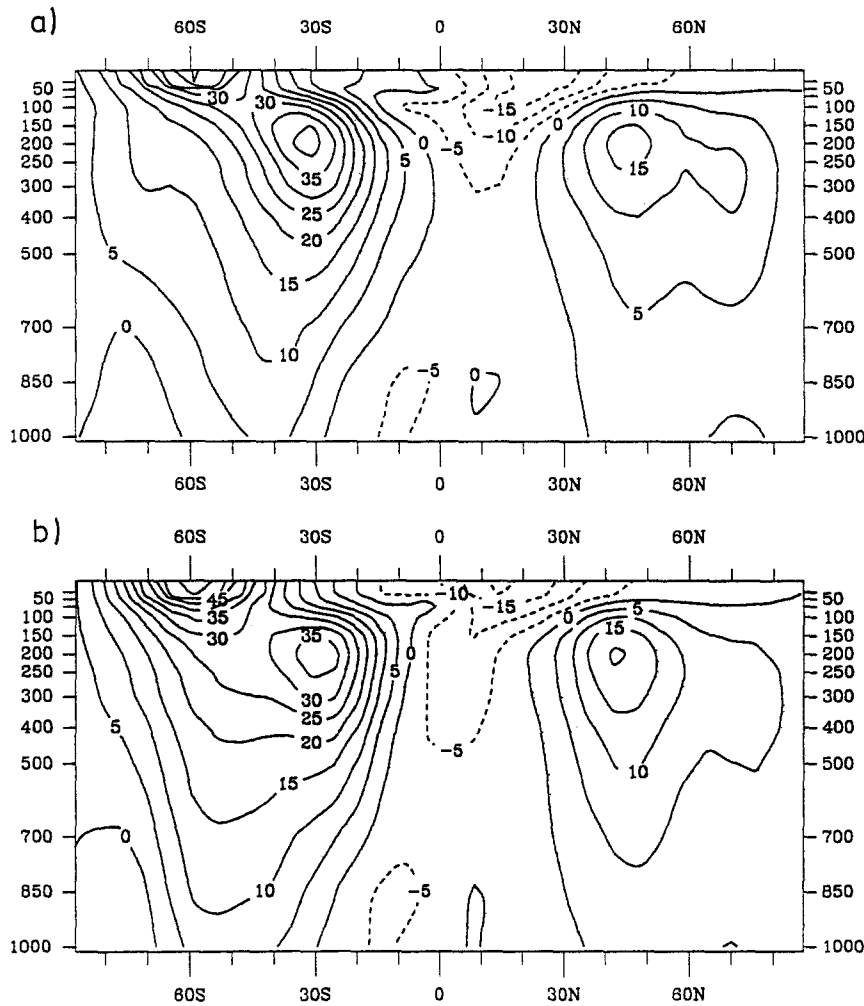
Fig. 5a, b. Zonally-averaged profile of the zonal wind component (m/s) for the summer season (JJA) in the final decade (years 91–100) a of the control simulation and b in the observations. The observed data are based on ECMWF analyses from 1979–88
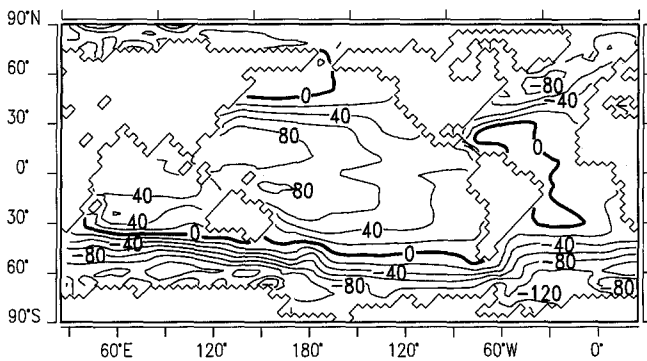
Fig. 6. Mean sea level with respect to an equipotential surface (cms). Results are for the final decade (years 91–100) of the control run

In the deep Pacific, the structures are much more homogeneous than in the Atlantic. In the upper 1000 m, the pattern is dominated by the high salinity in the subtropical gyres. The observed data show a slight salinity minimum in the Southern Ocean, which is not reproduced by the model (see also Maier-Reimer et al. 1992).

Figure 9a shows the integrated heat flux into the ocean as a function of latitude for the global ocean and individual ocean basins for the final decade of the con-

trol run. The meridional heat transports were computed from the appropriate zonally integrated air-sea heat fluxes assuming a stationary ocean circulation, with zero transports at the north pole (or northern ocean boundary). Since the ocean was, in fact, slowly cooling in the control run, the meridional fluxes at the south pole are not exactly zero, as they would be for a stationary ocean. The general structure agrees reasonably well with current estimates from observations (see Fig. 9b; after Talley 1984). Outside the equatorial Ekman cell the poleward heat transport in the Northern Hemisphere is dominated by the North Atlantic heat transport of 0.8×10^{15} W at 45°N. The differences between the Atlantic and the other oceans clearly reveal the operation of the conveyor belt circulation, which transports 25 Sv of NADW from the Atlantic into the Southern Ocean across 30°S. The computed transport lies within the range of independent estimates from observations (Roemmich 1980; Hall and Bryden 1982; Gordon and Piola 1983; Hsiung 1985), but nearer the lower values.

A particularly sensitive component of the coupled atmosphere-ocean model is the sea ice. The flux correction technique is only partially effective in the ocean-ice transition zone, the control run requiring about 60 years for the sea ice distribution to equilibrate. During this initial period the annual cycle is exaggerated in the Arctic, with
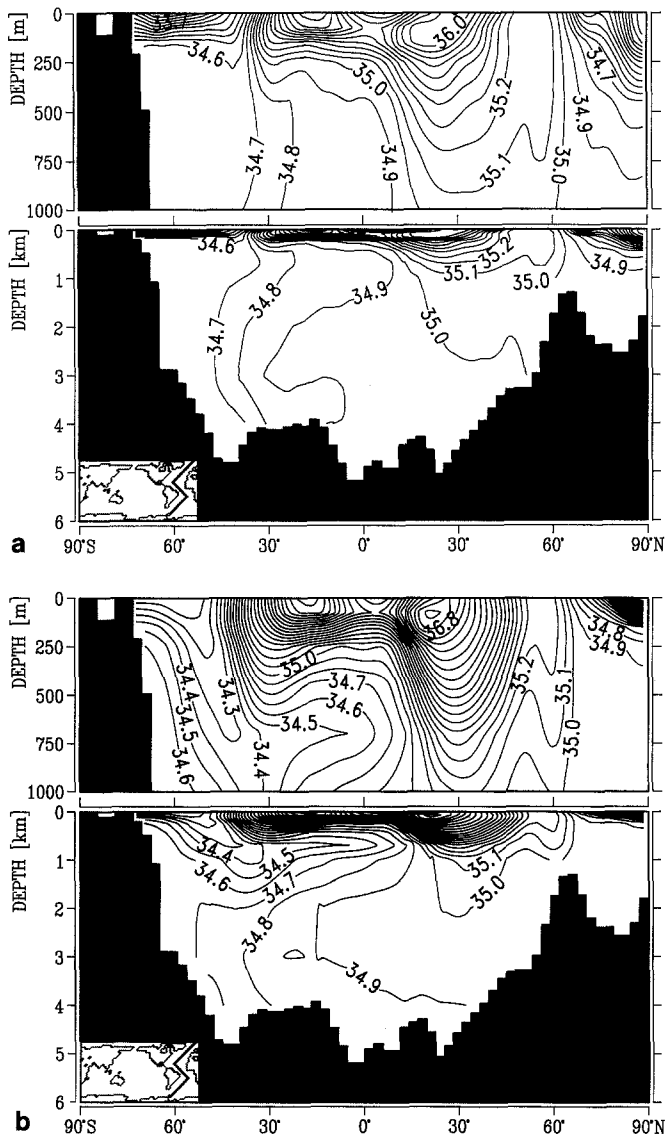
Fig. 7. a Cross-section of salinity (per mille) along a transect through the central Atlantic (see inset) for the final decade (years 91-100) of the control integration. The *upper panel* shows results for the top 1000 m of the ocean; b Cross-section of salinity (per mille) along the same transect as in a for the Levitus (1982) data set
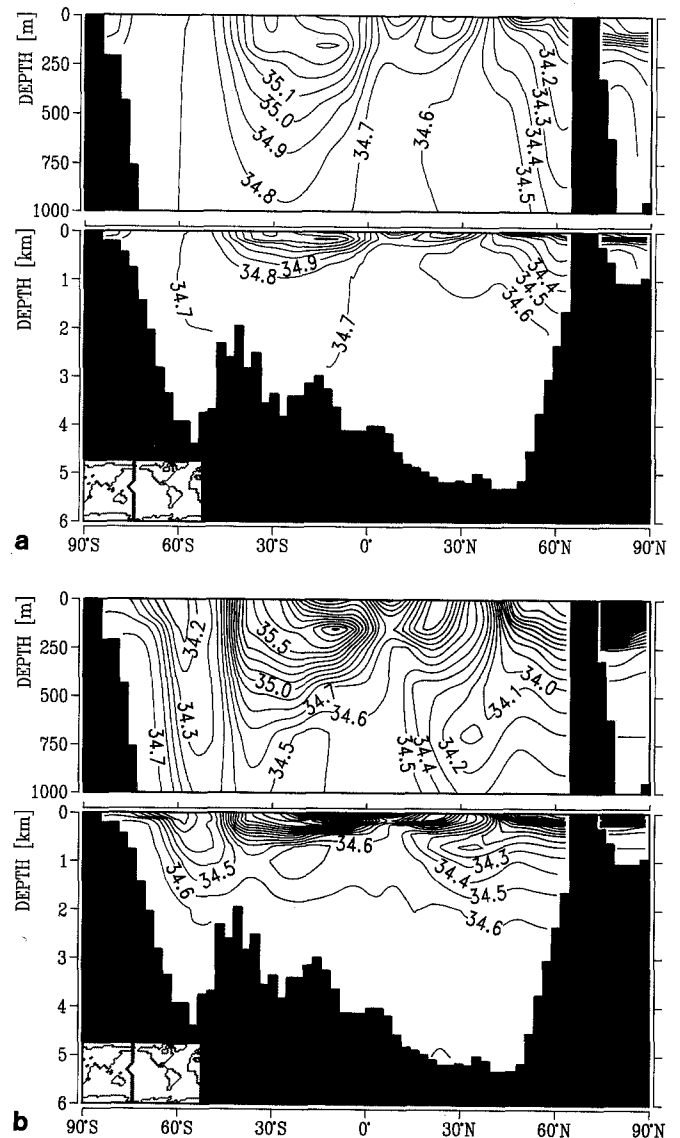
Fig. 8. a Cross-section of salinity (per mille) along a transect through the central Pacific (see inset) for the final decade (years 91-100) of the control integration. The *upper panel* shows results for the top 1000 m of the ocean; b Cross-section of salinity (per mille) along the same transect as in a for the Levitus (1982) data set

almost ice-free conditions in summer and refreezing in winter. Subsequently the seasonal distribution of sea ice in the control run appears reasonably realistic.

The control run is quasi-stationary with respect to the global mean near surface temperature, drifting by less than 0.4 K during the 100-year integration (Fig. 10). The spatial temperature distribution, however, shows some drift, with high-latitude cooling in the north and warming in the south. The root mean square of the area-weighted temperature anomaly for the final decade of the control run (relative to the control run initial state) is 1.1 K. Since the coupled ocean-atmosphere model, like the real climate system, can be expected to exhibit natural fluctuations on time scales of a century and longer (Mikolajewicz and Maier-Reimer 1990), it is difficult to determine whether the observed high-latitude non-sta-

tionarity of the control run represents the real natural variability of the coupled system or a spurious residual drift due to incomplete drift compensation by the flux correction. To resolve this question unambiguously, significantly longer integrations are needed than were possible for this study.

The changes occurring in the present 100-year control run are nevertheless consistent with the low-frequency variability found in a several thousand year integration of the LSG ocean model, in which the ocean was forced by short-term surface flux variations characteristic of natural atmospheric weather variability (Mikolajewicz and Maier-Reimer 1990). The simulated ocean circulation exhibited a pronounced red-noise variability typical of observed climate variations, the variance spectra of the oceanic heat transport and other characteristic circu-
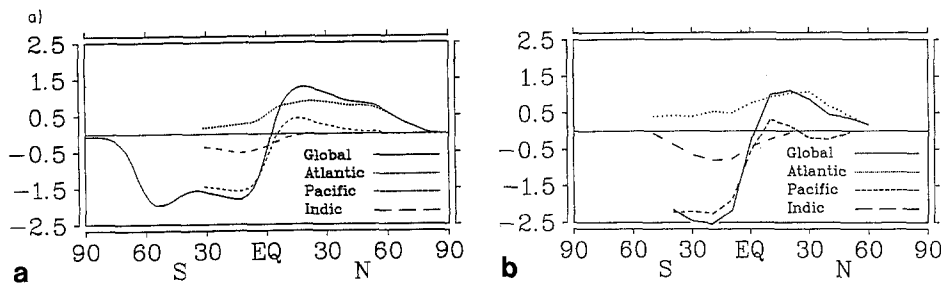
Fig. 9a, b. Integrated heat flux into the ocean (PW), given as a function of latitude and separately for the global ocean and individual ocean basins. Results are shown for the final decade (years 91–100) a of the control run and b for observations from Talley (1984)
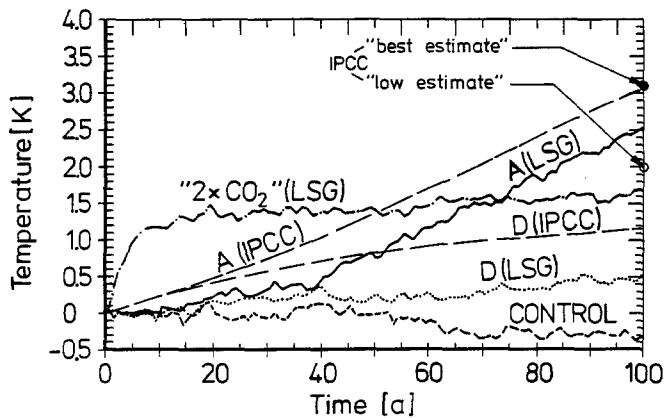

Fig. 10. Time evolution of the global mean near surface temperature change (°C) for the three greenhouse warming simulations, the control experiment and the IPCC "best estimates"

lation indices increasing monotonically towards low frequencies for time scales up to several centuries. We shall, accordingly, interpret the non-stationary behaviour of the control run in the first instance as inherent internal variability of the coupled model. Assuming that the natural variability arising in the control run and the response simulations are uncorrelated, we define the time-dependent climate response in the greenhouse warming simulations as the deviation with respect to the smoothed initial state of the system, as given by the average of the first ten years of the control run (definition 1). However, we shall discuss also the alternative possibility that the control run changes represent a spurious drift or a component of the natural variability which is common to all simulations. In this case it is more appropriate to define the climate response as the instantaneous difference between the greenhouse simulation and the control run at the same time instance (definition 2).

Greenhouse warming simulations

Figure 10 shows the evolution of the global mean temperature increase, in accordance with our definition 1, for the three greenhouse warming simulations (the change according to definition 2 can be also be seen from the instantaneous difference relative to the control run). Since the coupled model can only explicitly consider the radiative effects of CO_2, the combined radiative forcing of CO_2 and all other greenhouse gases is expressed in terms of an equivalent atmospheric CO_2 con-

centration, as in IPCC (Houghton et al. 1990). Note that our $2 \times CO_2$ value of 720 ppm equivalent CO_2 represents a doubling of the equivalent CO_2 concentration relative to the level of the early 1980s, rather than 1985. The precise definition of $2 \times CO_2$ is immaterial for our purposes.

The response of the $2 \times CO_2$ experiment shows a characteristic two-time-scale structure (see also Manabe et al. 1990). An initial rapid temperature increase by approximately 1 K within 5 years is followed by a more gradual linear increase to a net increase of about 1.7 K after 100 years, with no sign of saturation. This is consistent with the separate time scales of the upper ocean (time scales of a few months for the mixed-layer to about a decade for the main thermocline) and the abyssal ocean (time scales of several hundred to a thousand years).

In Scenario A the temperature increases by only 0.5 K during the first 40 years, but the curve then steepens to a growth rate of ca. 0.36 K per decade to reach 2.6 K after 100 years. The temperature increase after 100 years integration for Scenario D is less than 0.6 K. The results for the latter stages of these two integrations lie between the IPCC "best" and "low estimates" (Houghton et al. 1990) based on a simple box-diffusion-upwelling model (definition 2, in which the instantaneous control run is subtracted from the greenhouse simulations, is seen to yield close agreement with the IPCC "best estimates" after 100 years). However, the temperature increase during the first 50 years is consistently lower for both Scenarios A and D than for the corresponding IPCC values (independent of the response definition). It is of interest that a similar coupled model simulation at the Hadley Centre showed a comparable depression (Houghton et al. 1992), although another simulation with a coupled ocean-atmosphere model by the Princeton group (Manabe et al. 1991) yielded an approximately linear increase without an initial depression.

A plausible explanation for much of the delayed warming is the lack of a warm-up in our simulations for the period prior to 1985: the experiment was started in 1985 from an initial equilibrium state rather than from an already warming state. An initial analytical estimate of this "cold start" error based on the impulse-response characteristics of the coupled system inferred from the $2 \times CO_2$ simulation yielded a small error of less than 0.1 K. However, a test of the linear response function inferred from the $2 \times CO_2$ experiment by applying it to compute the temperature increase for Scenario A revealed significant deviations from the full coupled
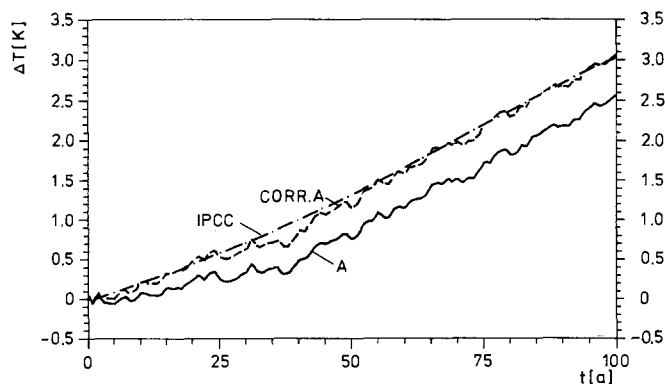
Fig. 11. Original and cold start corrected global mean temperature increase (°C) for Scenario A, together with the IPCC "best estimates" (after Hasselmann et al. 1992)

ocean-atmosphere model simulation (we are grateful to U. Siegenthaler, who carried out this computation independently, for stressing the significance of this deviation and to the comments of T. M. L. Wigley and the referees, which motivated us to re-examine our first results). We accordingly derived the effective linear input re-

sponse function instead from the Scenario A computation itself. The application of this, we hope more consistently defined response function, yielded a significantly larger cold start error of 0.4 K after 50 years. Details of the computation are given in Hasselmann et al. (1992).

Figure 11 shows the original and cold-start-corrected global mean temperature increase for Scenario A, indicating that most, but not quite all, of the delayed warming relative to the IPCC prediction can be explained by the cold start correction. It should be stressed, however, that due to natural variability of the coupled ocean-atmosphere system (see Mikolajewicz and Maier-Reimer 1990), there is considerable uncertainty involved in estimating the impulse response characteristics of the model from a single experiment. A number of experiments starting from different initial conditions would be desirable in order to reduce the uncertainties associated with this estimate.

Evolution of surface temperature distributions

Figure 12a shows the global distribution of the decadal mean near surface temperature change (according to
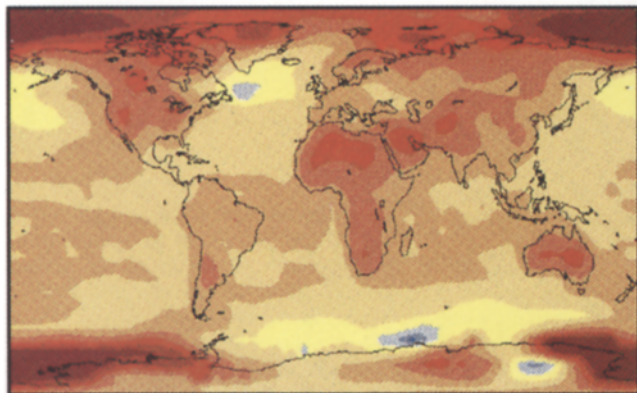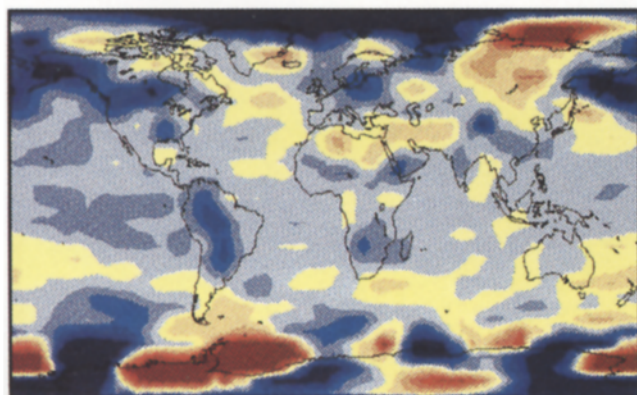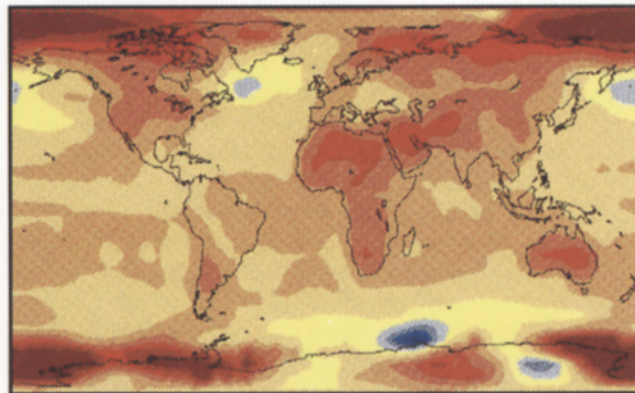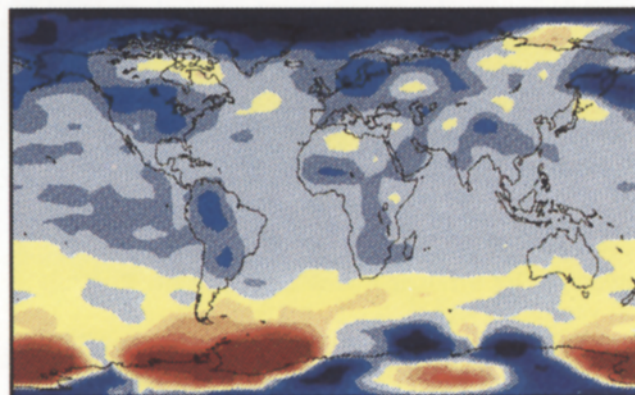
Fig. 12. a Distribution of the change in annually-averaged near surface temperature for the final decade (years 91–100) of the Scenario A integration relative to the initial state (average over years 1–10) of the control run; **b** EOF 1 of the annually-averaged near surface temperature changes for Scenario A. The explained variance is 84.1%; **c** EOF 2 of the annually-averaged near surface temperature changes for Scenario A. The explained variance is 3.1%; **d** EOF 1 of the annually-averaged near surface temperature changes for the control run. The explained variance is 52.5%

definition 1) in the last decade of the integration for Scenario A. The warming over the oceans is strongly reduced relative to the continents; some ocean areas (e.g., the North Atlantic) even show a cooling. Compared with earlier atmosphere-mixed-layer model simulations (Schlesinger and Mitchell 1987; Mitchell et al. 1990), the land-sea contrast is more pronounced, indicating an enhanced heat uptake by the oceans below the mixed-layer. There is also an attenuation of the response in the Southern Hemisphere, a feature observed only in coupled ocean-atmosphere models (e.g., Washington and Meehl 1989a; Stouffer et al. 1989; Manabe et al. 1991; Houghton et al. 1992). The largest temperature increases (up to ca. 12 K) occur where the sea ice retreats, particularly in the Arctic. The spatial patterns of the temperature change for Scenario D and the $2 \times CO_2$ experiment (not shown) are very similar, but of smaller amplitude.

To gain more insight into the space-time structure of the transient temperature response, an eigenvector (empirical orthogonal function: EOF) analysis was carried out. The EOFs were computed separately for the control run and each greenhouse warming experiment using the full 100 years of data, with anomalies defined according to our definition 1. EOFs were formed using area-weighted spatial averages, without subtraction of the time means (since we were interested in the full signals), and were normalized to define an orthonormal basis.

More than 87.2% of the (time and space averaged) mean square signal for Scenario A can be explained by only two patterns (Fig. 12b and c). The first EOF (Fig. 12b) already explains 84.1% of the variance, and contributes over 95% of the spatial variance of the signal in the last decade of the experiment (note the close similarity between Fig. 12 a and b).

The first two EOFs of the other simulations also explain most of the variance: 59.2% for Scenario D, 90.5% for the CO_2 doubling experiment and 71.2% for the control run. The first EOF patterns in all three greenhouse warming experiments are very similar, with spatial pattern correlations of 0.82 for A versus D and 0.97 for A versus $2 \times CO_2$ (note that all pattern correlations were computed with subtraction of the spatial means, as in Wigley and Santer 1990). In contrast, the first EOF of the control run (52.5% explained variance; Fig. 12d), which is associated mainly with the strong variability at high soutern latitudes, has only a weak resemblance to these patterns: the correlation with EOF 1 of Scenario A is only 0.43. Thus, the dominant greenhouse warming pattern of the three response experiments cannot have been strongly affected, in the space-time average, by a possible common spurious drift or natural variability signal.

EOF 2 of Scenario A, however, although contributing only 3.1% to the variance, is rather similar to EOF 1 of the control run (pattern correlation $r = 0.74$; see Fig. 12c, d). Thus, this component of the greenhouse warming signal could contain a spurious drift or natural variability contribution. This is supported by the strong variability exhibited by this pattern in the vicinity of the Antarctic Circumpolar Current, a relatively unstable region of the ocean circulation in which a similar variabil-

ity was found also in the stochastically forced ocean experiment of Mikolajewicz and Maier-Reimer (1990). However, it should be noted that the patterns of natural variability and the response of the system to external forcing often tend to be similar, since important features of both signal and noise patterns can be established via common feedback mechanisms (e.g., ice-albedo feedback). A high pattern correlation in itself, therefore, is not necessarily evidence of a contamination of the greenhouse warming signal by natural variability noise (Liu and Schuurmanns 1990).

The relation between the greenhouse signal and the natural variability or drift of the coupled model becomes clearer if the evolution of the patterns with time is considered. Figure 13 shows the evolution of the cumulative EOF contributions to the explained spatial var-
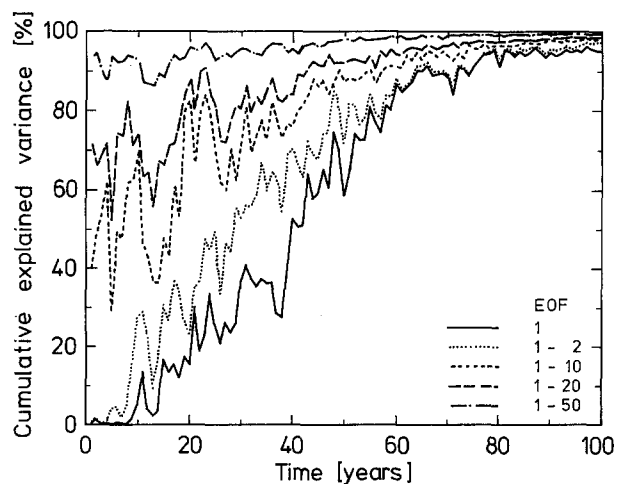

Fig. 13. Cumulative explained spatial variance as a function of time and number of EOFs (1, 2, 10, 20 and 50) for Scenario A. The signal is defined as the difference relative to the smoothed initial state (average over years 1–10) of the control run. Results are for annually averaged 2 m temperature
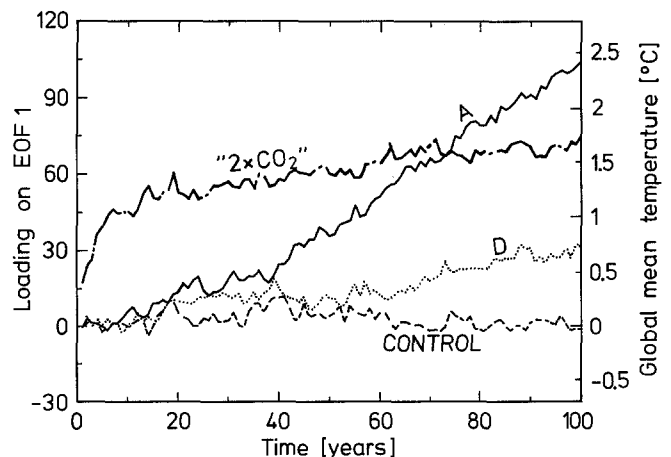
Fig. 14. Principal component time series for the projection of the temperature response fields of the three greenhouse warming experiments and the control run onto EOF 1 of Scenario A. The *ordinate axis* on the *right hand side* of the figure indicates the contribution of EOF 1 to the global mean temperature (cf. Fig. 10)

iance for Scenario A. The contribution from the first EOF is seen to grow monotonically, completely dominating the greenhouse warming pattern towards the end of the integration. There is little doubt that the first EOF represents a real signal, since, as pointed out, essentially the same pattern is found in all three greenhouse experiments and the pattern is not strongly correlated with the dominant variability pattern of the control run.

In the first half of the Scenario A experiment, however, the response is composed of many EOF patterns. The contribution from the second EOF in this period is comparable to that of EOF 1, and both patterns initially represent only a small fraction of the total spatial variance. The relative contribution from EOF 2 is largest in the fourth decade, during the transition from the slow to the more rapid temperature response regime (see Fig. 10). Since, as just discussed, the EOF 2 pattern is the one which is most prone to contamination by natural variability, we repeated the analysis using definition 2 for the greenhouse response (subtraction of the instantaneous rather than the initial control run state from the greenhouse simulation). This did not reduce the EOF 2 contribution: the cumulative variance curves were found to be similar to those of Fig. 13, with an even stronger EOF 2 signal in decades 3-5.

To compare the temporal evolution of the spatial response patterns of the three greenhouse simulations and the control run on a common basis, the signals (according to definition 1) of all experiments were projected onto the EOFs of Scenario A. The coefficient (principal component) time curves for the projection on EOF 1

(Fig. 14) support our previous conclusion that most of the signal can be explained by a single common pattern in all three greenhouse experiments, while the coefficient of this pattern for the control run is small. The similarity of the curves in Fig. 14 with those in Fig. 10 (global mean temperature) is explained by the fact that the first EOF largely determines the global mean temperature: the spatial mean of EOF 1 is almost five times larger than that of EOF 2; the contribution of EOF 1 to the global mean temperature is indicated by the ordinate axis on the right hand side of Fig. 14.

Temperature sections

Vertical sections of the temperature anomaly distribution (according to definition 1) established in the last decade of the integration for Scenario A are shown in Fig. 15a (atmosphere) b and c (ocean). The warming in the atmosphere is largest in the tropical tropopause (Fig. 15a) and at the surface at high latitudes, while the stratosphere shows, as expected, an extensive cooling. The largest warming of the oceans takes place in the uppermost levels, with a maximum of more than 2 K in the tropical regions. The warming penetrates into the deep ocean in the high latitude regions of deep convection, mainly the Northern Atlantic, the Weddell Sea and the Ross Sea (Fig. 15b, c). These regions generally coincide with the regions of low warming or even cooling at the surface (Fig. 15a, see also Stouffer et al. 1989).

The stabilization of the water column through surface warming tends to suppress deep convection. This
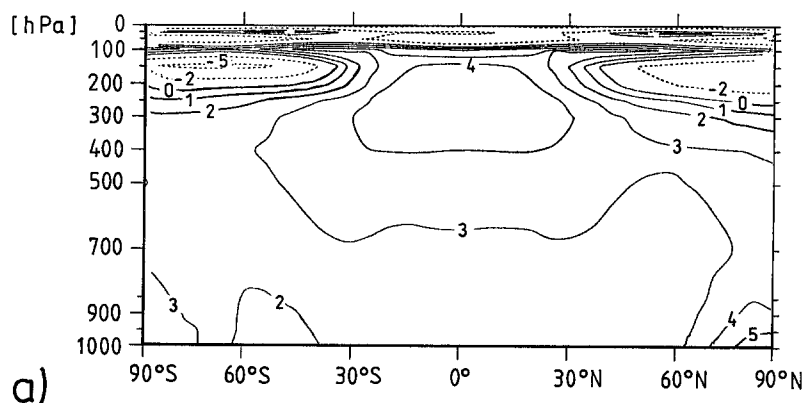
Fig. 15a–c. Vertical cross-section of zonally averaged changes (°C) a in atmospheric temperature a and b vertical cross-section of temperature changes along transects in the central Atlantic and c central Pacific. Results are for the final decade (years 91–100) of Scenario A relative to the smoothed initial state (average over years 1–10) of the control run
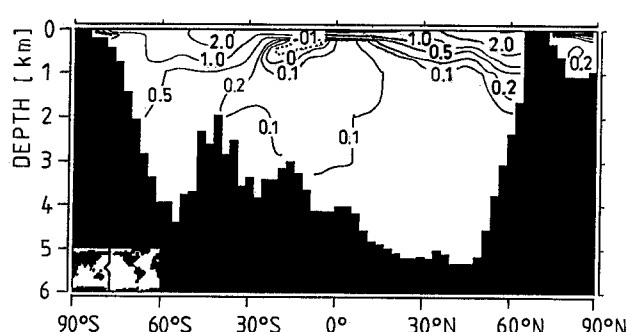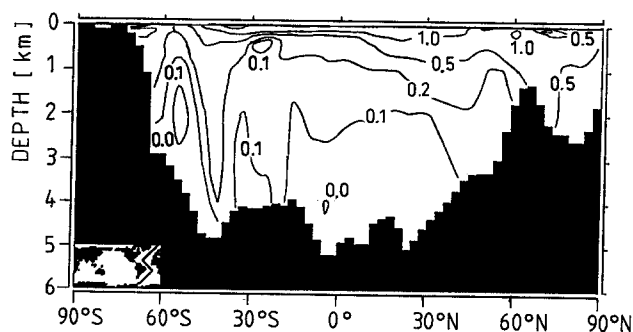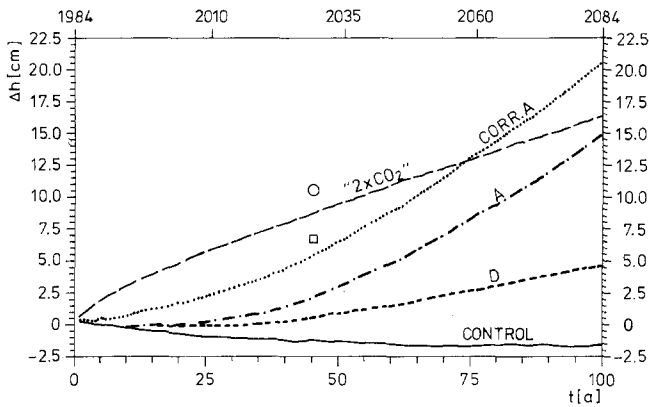
Fig. 16. Time evolution of global mean sea level changes (cms) due to thermal expansion of the ocean in the two IPCC scenarios, the $2 \times CO_2$ experiment and the control run. The IPCC estimates for Scenario A (thermal expansion effects only) in 2030 are marked. The Scenario A sea level rise after correction for the "cold start" depression (Hasselmann et al. 1992) is also shown

inhibits the mean convective heat flux from the deep ocean to the surface in high latitudes, counteracting the surface ocean greenhouse warming in these regions. In Scenario A, the global deep water formation is reduced by about 30% at the end of the experiment, with a corresponding retardation of the thermohaline circulation. The resulting longer surface exposure time produces a positive surface salinity anomaly in regions of high evaporation in the subtropical gyres and a negative surface salinity anomaly in high latitude precipitation regions, for example in the North Atlantic (Mikolajewicz et al. 1990). The reduction in the global overturning of the ocean could potentially reduce the uptake rate of CO_2 in the ocean (Maier-Reimer and Hasselmann 1987), producing a positive greenhouse warming feedback.

Evolution of sea level

An important consequence of global warming is the sea level rise due to the melting of glaciers, changes in the components of the hydrological cycle (precipitation, evaporation and runoff), and the thermal expansion of the ocean. The first effect is not included in our model. The second effect is very small, of the order of 1 or 2 cm. We discuss here only the third contribution. This is also relatively modest in our 100-year simulations. The global mean sea level rise after 100 years due to thermal expansion only is computed as 15 cm for Scenario A, 5 cm for Scenario D and 16 cm for the $2 \times CO_2$ experiment (Fig. 16). The larger sea level rise in the $2 \times CO_2$ experiment, despite a smaller final temperature increase than in Scenario A (Fig. 10), requires further explanation.

The sea level rise $S(t)$ due to the thermal expansion of the ocean can be represented generally for a linear system by the response integral:

$$S(t) = \int_0^t P(u)\, G(t-u)\, du$$

where $p(u)$ represents the rate of increase of the radiative forcing due to the increase in the atmospheric CO_2 concentration and $G(u)$ represents the response to a unit step function increase in radiative forcing (assumed to be proportional to the logarithm of the CO_2 concentration) at time $u = 0$.

The response function $G(u)$ can be determined empirically from the global warming simulation with the coupled ocean-atmosphere model. In contrast to the response function for the global mean temperature, the sea level response functions determined from the $2 \times CO_2$ and Scenario A experiments were found to be very similar (Hasselmann et al. 1992), and can be represented by a single exponential (where in this case the second definition of the response is used, however, to avoid the obvious initial internal oscillation seen in the sea level of the control run; see Fig. 16).

The time constant of about 100 years is determined by the warming of the deep ocean. The structure of the thermal expansion can be seen in Fig. 17 and 18, which show the vertical integral of the thermal expansion, in centimeters, from the bottom to a given level in cross sections through the central Atlantic and Pacific, respectively, during the final decade of the $2 \times CO_2$ (Figs. 17a, 18a) and Scenario A (Figs. 17b, 18b) experiments. The larger bottom-to-top thermal expansion, i.e., net sea level rise in the $2 \times CO_2$ experiment is seen to be caused by the more effective warming of the deep ocean. This is due to the longer impact time of the sudden heat flux increase at time $t = 0$ in this experiment compared with the slower increase of Scenario A.

Non-uniform warming and dynamical effects generally yield variations in the spatial pattern of sea level rise in both experiments of the same order as the global mean (Mikolajewicz et al. 1990). Regional differences between the sea level response of the two experiments can be explained by the varying time scales of different regions of the ocean, which affects the response for a slow or rapid increase in CO_2.

The contribution to the sea level response is comparable in both experiments for the more rapidly responding parts of the ocean, such as the upper 500 m in the subtropical gyres or the entire water column of the Arctic Ocean, while in most of the deep ocean the thermal expansion for the $2 \times CO_2$ experiment is significantly larger than for Scenario A.

The simulated mean sea level rise due to thermal expansion is approximately half that of the IPCC projections (Fig. 16). This largely reflects the slower temperature response in the first half of our Scenario A and D experiments relative to the corresponding IPCC estimates (see Fig. 10). However, comparing the sea level rise after correction for the "cold start" depression (see Fig. 16; after Hasselmann et al. 1992) with the cold start corrected temperature curve in Fig. 11, it appears that the ratio of sea level rise to temperature rise is inherently somewhat lower in our coupled model experiment than in the IPCC estimate based on a box-diffusion-upwelling model.

Published estimates of the equilibrium global sea level rise due to the thermal expansion of the oceans for the
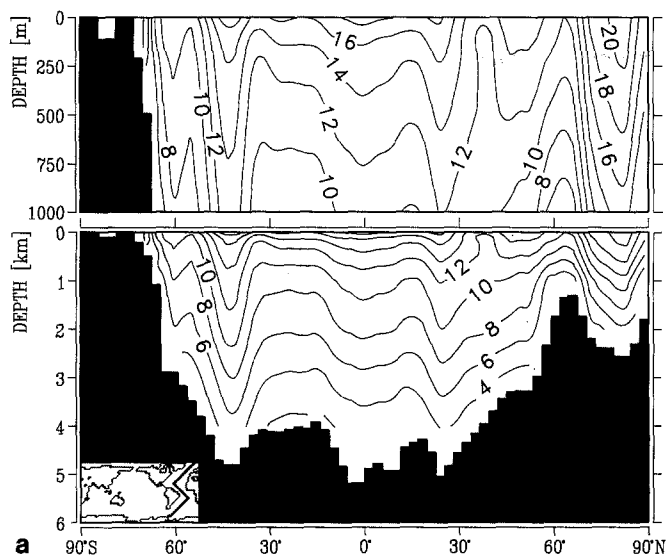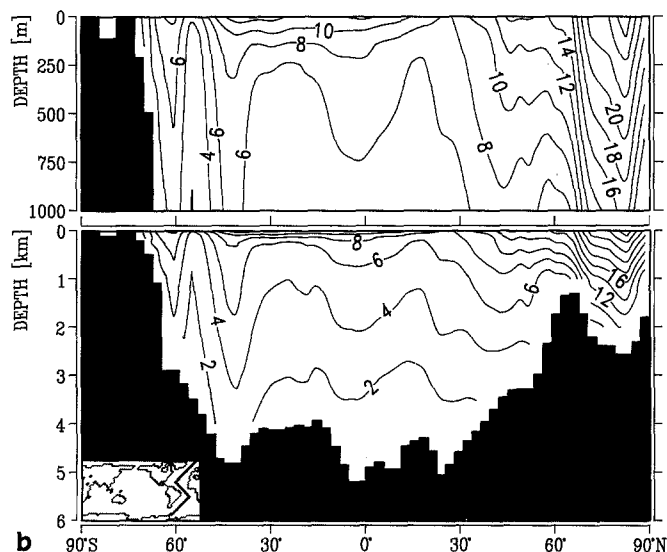
Fig. 17a, b. Bottom-to-top integral of the thermal expansion in centimeters (in a cross-section through the central Atlantic) during a the final decade of the $2 \times CO_2$ and b Scenario A experiments


Fig. 18a, b. Bottom-to-top integral of the thermal expansion in centimeters (in a cross-section through the central Pacific) during a the final decade of the $2 \times CO_2$ and b Scenario A experiments

equilibrium climate response to a CO_2 doubling generally lie in the range of 50 cm. Our significantly lower estimates for the transient sea level response within one century are not inconsistent with these predictions and are supported by the time dependent sea level computation in a 2000-year integration made with the LSG ocean model (Mikolajewicz et al. 1990). The simulation yielded an asymptotic sea level rise due to thermal expansion of approximately 50 cm, in accord with the IPCC estimates. However, the increase in sea level was found to be a very slow process requiring several hundred years adjustment time, with the increase during the first hundred years of the same order as found here.

Conclusions

Simulations with a global coupled atmosphere-ocean model of the greenhouse warming over the next 100 years for the IPCC Scenarios A ("business as usual") and D ("accelerated policies") and a $2 \times CO_2$ experiment support the order of magnitude predictions of the IPCC report (Houghton et al. 1990). The global average near-surface temperature increase of 2.6 K in Scenario A and 0.6 K in Scenario D at the end of the simulation lie close to the IPCC "best estimate". However, the global average temperature changes in years 10–50 of Scenarios A and D are consistently lower than the corresponding IPCC values. Most of this delay could be explained by the lack of a warm-up period prior to the start of the integration, but a part could also be due to the stronger oceanic heat uptake resulting from a more realistic description of the deep ocean in the present model. Pro-

nounced warming occurs in the deep ocean in high latitude regions of penetrative convection, mainly in the Northern Atlantic, the Weddell Sea and the Ross Sea. These areas coincide with regions of low warming or even initial cooling at the surface, a feature which cannot be simulated by models with mixed-layer oceans. Additionally, the differences in the forcing histories of the Scenario A and $2 \times CO_2$ experiments yield marked differences in the vertical temperature structure of the ocean.

A single common temperature response pattern establishes itself as the dominant climatic signal in the later stages of all three greenhouse experiments. It is characterized by a significantly larger warming over land areas than over oceans, and a corresponding attenuation of the warming in the Southern Hemisphere. This pattern can be clearly distinguished from the internally-generated natural variability (or possibly residual drift) in the control run. In the first 50 years of the simulation, however, the greenhouse signal contains additional patterns of comparable magnitude which cannot be so clearly separated from the model's natural variability.

The global sea level rise due to the thermal expansion of the ocean is only 15 cm after 100 years for Scenario A, 5 cm for Scenario D and 16 cm for the CO_2 doubling experiment. These values are half as large as the corresponding IPCC estimates and can be only partly explained by the cold start error. It appears that the coupled model yields a smaller ratio of the sea level rise relative to the temperature increase than the box-diffusion-upwelling models. Regional variations in sea level rise due to variations in warming and dynamic effects are of the same order as the global mean. Our smaller sea level rise values imply only a delay in the sea level response arising from the thermal expansion of the oceans and are not inconsistent with previous estimates (Wigley and Raper 1987; Houghton et al. 1990; Mikolajewicz et al. 1990) of an asymptotic equilibrium thermal sea level rise of 50 cm for a CO_2 doubling.

References

Bakan S, Chlond A, Cubasch U, Feichter J, Graf H, Graßl H, Hasselmann K, Kirchner I, Latif M, Roeckner E, Sausen R, Schlese U, Schriever D, Schult I, Schumann U, Sielmann F, Welke W (1991) Climate response to smoke from the burning oil wells in Kuwait. Nature 351:367–371

Boer GJ, Arpe K, Blackburn M, Deque M, Gates WL, Hart TL, Le Treut H, Roeckner E, Sheinin DA, Simmonds I, Smith

RNB, Tokioka T, Wetherald RT, Williamson D (1991) An intercomparison of the climates simulated by 14 atmospheric general circulation models. WMO/TD-No 425, Geneva

Cess RD, Potter GL, Blanchet JP, Boer GJ, Ghan SJ, Kiehl JT, Le Treut H, Li ZX, Liang XZ, Mitchell JFB, Morcrette J-J, Randall DA, Riches MR, Roeckner E, Schlese U, Slingo A, Taylor KE, Washington WM, Wetherald RT, Yagai I (1989) Interpretation of could climate feedback as produced by 14 atmospheric general circulation models. Science 245:513–516

Broecker WS (1987) The biggest chill. Nat Hist Mag 97:74–82

Gordon AL (1986) Interocean exchange of thermocline water. J Geophys Res 91:5037–5046

Gordon AL, Piola AR (1983) Atlantic Ocean upper layer salinity budget. J Phys Oceanogr 13:1293–1300

Hall MM, Bryden HL (1982) Direct estimates and mechanisms of ocean heat transport. Deep-Sea Res 29A:339–359

Hansen J, Fung I, Lacis A, Rind D, Lebedeff S, Ruedy R, Russell G, Stone P (1988) Global climate changes as forecast by Goddard Institute for Space Studies three-dimensional model. J Geophys Res 93:9341–9364

Hasselmann K (1991) Ocean circulation and climate change. Tellus 43 AB:82–103

Hasselmann K, Sausen R, Maier-Reimer E, Voss R (1992) On the cold start problem in transient simulations with coupled ocean-atmosphere models. MPI Report No 83, MPI für Meteorologie, Hamburg, FRG

Houghton JT, Jenkins GJ, Ephraums JJ (1990) Climate change. The IPCC Scientific Assessment, Cambridge University Press, Cambridge

Houghton JT, Callander BA, Varney SK (1992) Climate changes 1992. The supplementary report to the IPCC assessment. Cambridge University Press, Cambridge

Hsiung J (1985) Estimates of global oceanic meridional heat transport. J Phys Oceanogr 15:1405–1413

Lautenschlager M, Herterich K (1990) Atmospheric response to ice age conditions – climatology near the Earth's surface. J Geophys Res 95:22547–22557

Levitus S (1982) Climatological atlas of the World Ocean. NOAA Professional Paper 13, 173 pp

Liu Q, Schuurmanns CJE (1990) The correlation of tropospheric and stratospheric temperatures and its effect on the detection of climate changes. Geophys Res Lett 17:1085–1088

Maier-Reimer E, Hasselmann K (1987) Transport and storage of CO_2 in the ocean – an inorganic ocean-circulation carbon cycle model. Clim Dyn 2:63–90

Maier-Reimer E, Mikolajewicz U (1989) Experiments with an OGCM on the cause of the Younger Dryas. In: Ayala-Castanares A, Wooster W, Yanez-Arancibia A (eds) Oceanography 1988. UNAM Press, Mexico, pp 87–100

Maier-Reimer E, Mikolajewicz U, Hasselmann K (1992) Mean circulation of the Hamburg LSG OGCM and its sensitivity to the thermohaline surface forcing. J Phys Oceanogr (accepted)

Manabe S, Bryan K, Spelman MJ (1990) Transient response of a global ocean-atmosphere model to a doubling of carbon dioxide. J Phys Oceanogr 20:722–749

Manabe S, Stouffer RJ, Spelman MJ, Bryan K (1991) Transient responses of a coupled ocean-atmosphere model to gradual changes of atmospheric CO_2. Part I: annual mean response. J Climate 4:785–818

Mikolajewicz U, Maier-Reimer E (1990) Internal secular variability in an ocean general circulation model. Clim Dyn 4:145–156

Mikolajewicz U, Santer BD, Maier-Reimer E (1990) Ocean response to greenhouse warming. Nature 345:589–593

Mitchell JFB, Manabe S, Tokioka T, Meleshko V (1990) Equilibrium climate change. In: Houghton JT, Jenkins GJ, Ephraums JJ (eds) Climate change. The IPCC Scientific Assessment, Cambridge University Press, Cambridge, pp 131–172

Roeckner E, Dümenil L, Kirk E, Lunkeit F, Ponater M, Rockel B, Sausen R, Schlese U (1989) The Hamburg version of the ECMWF model (ECHAM). In: Boer GF (ed) Research activi-

ties in atmospheric and oceanic modelling. CAS/JSC Working Group on Numerical Experimentation 13:7.1-7.4 WMO Technical Document 322, Geneva

Roemmich D (1980) Estimation of meridional heat flux in the North Atlantic by inverse methods. J Phys Oceanogr 10:1972-1983

Sausen R, Barthel K, Hasselmann K (1988) Coupled ocean-atmosphere models with flux corrections. Clim Dyn 2:154-163

Schlesinger ME, Mitchell JFB (1987) Climate model simulations of the equilibrium climatic response to increased carbon dioxide. R Geophys 25:760-798

Stouffer RJ, Manabe S, Bryan K (1989) Interhemispheric asymmetry in climate response to a gradual increase of atmospheric CO_2. Nature 342:660-662

Talley LD (1984) Meridional heat transport in the Pacific Ocean

Tibaldi S, Tosi E (1991) Low frequency variability and blocking as diagnostic tools for global climate models. In: Shukla J (ed) Proceedings of NATO Workshop on predictions of interannual climate variations. NATO/ASI Series, Trieste, 22-26/7/91

Washington WM, Meehl GA (1989a) Climate sensitivity due to increased CO_2: experiments with a coupled atmosphere and ocean general circulation model. Clim Dyn 4:1-38

Washington WM, Meehl GA (1989b) Seasonal cycle experiments on the climate sensitivity due to a doubling of CO_2 with an atmospheric general circulation model coupled to a simple mixed layer ocean model. J Geophys Res 89:9475-9503

Wetherald RT, Manabe S (1988) Cloud feedback processes in a general circulation model. J Atmos Sci 45:1397-1415

Wigley TML, Raper SCB (1987) Thermal expansion of seawater associated with global warming. Nature 330:127-131

Wigley TML, Santer BD (1990) Statistical comparison of spatial fields in model validation, perturbation and predictability experiments. J Geophys Res 95:851-865

Wilson CA, Mitchell JFB (1987) A doubled CO_2 climate sensitivity experiment with a global climate model including a simple ocean. J Geophys Res 92:13315-13343

Xu J-S, Storch H, van Loon H (1990) The performance of four spectral GCMs in the Southern Hemisphere: the January and July climatology and the semiannual wave. J Climate 3:53-70